applied sciences

MDPI

Article

Ge^{4+} Stabilizes Cu^{1+} Active Sites to Synergistically Regulate the Interfacial Microenvironment for Electrocatalytic CO_2 Reduction to Ethanol

Xianlong Lu [1,2,†], Lili Wang [1,2,3,†], Hongtao Xie [1], Zhendong Li [1], Xiangfei Du [1] and Bangwei Deng [1,2,*]

[1] Yangtze Delta Region Institute (Huzhou), University of Electronic Science and Technology of China, Huzhou 313001, China
[2] CMA Key Open Laboratory of Transforming Climate Resources to Economy, Chongqing 401147, China
[3] Institute of Fundamental and Frontier Sciences, University of Electronic Science and Technology of China, Chengdu 611731, China
* Correspondence: bwdeng@uestc.edu.cn
† These authors contributed equally to this work.

Abstract

Electrocatalytic conversion of CO_2 to high-energy-density multicarbon products (C_{2+}) offers a sustainable route for renewable energy storage and carbon neutrality. Precisely modulating Cu-based catalysts to enhance C_{2+} selectivity remains challenging due to uncontrollable reduction of $Cu^{\delta+}$ active sites. Here, an efficient and stable Ge/Cu catalyst was developed for CO_2 reduction to ethanol via Ge modification. A $Cu_2O/GeO_2/Cu$ core–shell composite was constructed by controlling Ge doping. The structure–performance relationship was elucidated through in situ characterization and theoretical calculations. Ge^{4+} stabilized Cu^{1+} active sites and regulated the surface microenvironment via electronic effects. Ge modification simultaneously altered CO intermediate adsorption to promote asymmetric CO–CHO coupling, optimized water structure at the electrode/electrolyte interface, and inhibited over-reduction of $Cu^{\delta+}$. This multi-scale synergistic effect enabled a significant ethanol Faradaic efficiency enhancement (11–20%) over a wide potential range, demonstrating promising applicability for renewable energy conversion. This study provides a strategy for designing efficient ECR catalysts and offers mechanistic insights into interfacial engineering for C–C coupling in sustainable fuel production.

Keywords: electrocatalytic CO_2 reduction; copper-based catalysts; germanium doping; C-C coupling; in situ spectroscopy

Academic Editor: Leonarda Liotta

Received: 17 September 2025
Revised: 20 October 2025
Accepted: 23 October 2025
Published: 24 October 2025

Citation: Lu, X.; Wang, L.; Xie, H.; Li, Z.; Du, X.; Deng, B. Ge^{4+} Stabilizes Cu^{1+} Active Sites to Synergistically Regulate the Interfacial Microenvironment for Electrocatalytic CO_2 Reduction to Ethanol. *Appl. Sci.* **2025**, *15*, 11420. https://doi.org/10.3390/app152111420

Copyright: © 2025 by the author. Licensee MDPI, Basel, Switzerland. This article is an open access article distributed under the terms and conditions of the Creative Commons Attribution (CC BY) license (https://creativecommons.org/licenses/by/4.0/).

1. Introduction

In recent years, the efficient utilization of CO_2 as a feedstock for sustainable fuels and chemicals has become a research hotspot for mitigating anthropogenic emissions [1]. CO_2 conversion strategies mainly include thermochemical, electrochemical, and photochemical methods. Among these, the electrochemical CO_2 reduction reaction (ECR) has attracted particular attention due to its ability to store intermittent renewable electricity from wind, tidal, and solar sources in chemical form, mild reaction conditions, flexible material selection (including catalysts, electrolytes, electrodes, and membranes), and broad process tunability [2]. Consequently, ECR has emerged as a key approach for producing carbon-based renewable fuels and chemicals while reducing dependence on fossil energy.

Specifically, ECR can convert the greenhouse gas CO_2 into high-value chemicals such as CO, CH_4, C_2H_4, and ethanol, thereby promoting sustainable energy utilization and supporting the achievement of carbon neutrality goals [3–5]. Among various catalysts, copper (Cu) is considered one of the most promising due to its unique electronic structure and moderate CO adsorption strength, enabling efficient production of C_{2+} products such as ethylene and ethanol [6,7]. Currently, there are a variety of Cu-based catalysts, including copper nanoparticles, copper oxides, copper alloys and surface-modified copper materials [8,9]. These catalysts exhibit different advantages in terms of activity, selectivity and stability, but the most promising for industrial application is still commercial copper with mass production, due to its low cost, wide source and mature processing. However, the catalytic performance of copper catalysts is significantly affected by their oxidation state and chemical valence, especially the presence of monovalent copper (Cu^{1+}) which is considered to be crucial for promoting the generation of C_{2+} products [10].

Copper oxides demonstrate enhanced activity and selectivity for producing C_{2+} products such as ethylene and ethanol [11]. This is mainly attributed to the fact that Cu^0 sites activate CO_2 and facilitate subsequent electron transfer, while Cu^{1+} sites enhance adsorption of CO (*CO) and promote C-C coupling [12]. The synergistic interaction between Cu^0 and Cu^{1+} significantly improves CO_2 activation and conversion to multicarbon products [13,14]. Recent studies have confirmed that the dynamic reversible conversion between Cu^0 and Cu^{1+} can be significantly stabilized in Cu-based catalysts by constructing oxide composite structures or organic ligand modification strategies [15–17]. However, multicarbon product formation is limited to a narrow potential window, as the catalysts exhibit CO_2 reduction behavior similar to that of a pure Cu catalyst at higher cathodic potentials [18]. Although construction of Cu^0-Cu^{1+} synergistic interfaces in heterogeneous materials (e.g., Cu/Cu_xS_x, Cu/CuPO) boost current density and selectivity, polysulfide or polyphosphate solubility causes instability at prolonged high redox potentials, increasing hydrogen evolution reaction (HER) and reducing the selectivity of the target product [19]. Therefore, effectively stabilizing Cu^{1+} species while suppressing HER remains a key challenge to improve Cu-based catalyst performance [20].

In this work, the ECR performance of GeO_x-modified commercial Cu catalyst was systematically investigated, revealing the mechanism of Ge species regulation on the dynamic structural evolution and catalytic performance of Cu catalyst. The catalysts prepared by the physical mixing-in situ reconfiguration strategy show a well-defined core–shell structure, with a GeO_x-Cu_2O composite interfacial phase formed on the surface of the Cu core. This interaction played an important role in stabilizing the Cu^{1+} species, thus effectively enhancing the ethanol selectivity. Ethanol produced on the Ge/Cu catalyst reached a maximum Faradaic efficiency of 47.8% at –0.8 V vs. RHE, which was 11.2% higher than that on pure Cu. Excessive Ge doping enhanced the HER, resulting in a decrease in ethanol Faradaic efficiency. The catalytic performance was optimal at a Ge doping level of approximately 15%. In order to explore the effect of GeO_2 on the stability of Cu^{1+} and its mechanism of regulating the pathway of ethanol generation, we employed advanced in situ characterization techniques to dynamically observe the structural evolution of the catalysts and the generation of intermediates. The structural features of the active centers were also analyzed in combination with non-in situ characterization. Density-functional theory (DFT) calculations were utilized to deeply explore the role of the introduction of Ge on the modulation of the electronic structure and reaction path of Cu. This study provides an important experimental and theoretical basis for optimizing the design of efficient and stable Cu-based catalysts.

2. Experimental Section

The experimental details, including material preparation, performance testing, in situ testing experiments and DFT calculations were summarized in Supporting Information (SI).

3. Results and Discussion

3.1. Synthesis and Characterization of Ge/Cu-Catalysts

A series of gas diffusion electrodes (GDEs) were prepared by making the catalysts into ink and spraying them on hydrophobic carbon paper. Scanning electron microscopy (SEM) was utilized to reveal the catalyst morphology and structure. The metallic germanium (Ge) showed a block structure (5.58 ± 2.18 μm) formed by the accumulation of small cubes with a particle size of 0.423 ± 0.208 μm (Figure S1), and EDS confirmed that the germanium element was uniformly distributed on the GDE. Copper (Cu) presented a spherical structure of 0.446 ± 0.092 μm, and elemental mapping showed uniform distribution of Cu and O (Figure S2). After ultrasonically mixing 15 wt% Ge powder with 75 wt% copper powder, the resulting Ge/Cu inherited the spherical characteristics of Cu (particle size of 0.436 ± 0.088 μm) and the germanium bulk structure was effectively dispersed, and EDS confirmed that the three elements of Cu, O, and Ge were uniformly distributed (Figure S3). The x wt% Ge/Cu samples with different germanium doping amounts (5–30 wt%) all maintained similar morphology and size characteristics (Figures S4 and S5). The process flow for the preparation of Ge/Cu composites was shown in Figure 1a, and the synthesis path was systematically optimized to ensure structural controllability. The high-resolution transmission electron microscopy (HRTEM) images of Figure S6 confirmed that the Ge/Cu catalysts exhibited a core–shell structure, in which the inner core was metallic Cu (marked in dark red) and the outer shell was Cu_2O and GeO_2 (marked in yellow), with the thickness of the shell layer of 72.3 nm. Figure 1b shows lattice spacings of 0.213, 0.296, and 0.246 nm, corresponding to the (200), (110), and (111) crystal facets of Cu_2O, respectively, while the 0.341 nm spacing matches the (101) facet of GeO_2. Selected Area Electron Diffraction (SAED) images further validated the HRTEM observations.

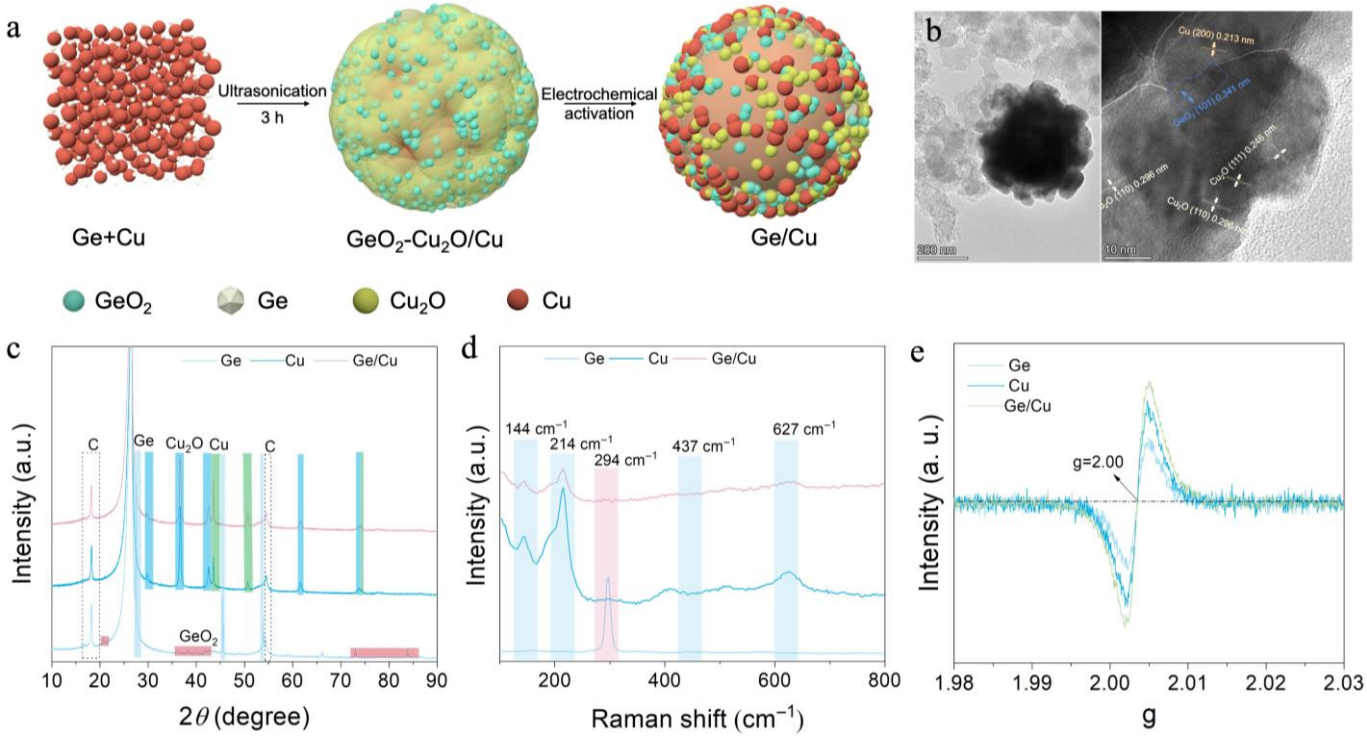

Figure 1. (**a**) Schematic diagram of catalyst preparation, (**b**) TEM images of Ge/Cu, (**c**) XRD patterns, (**d**) Raman spectrum, (**e**) EPR spectra.

Furthermore, the elemental distributions of Cu and O in the Energy-Dispersive X-ray Spectroscopy (EDS) images clearly show the structural features of the core–shell structure, while the Ge element is uniformly distributed in the shell layer. XRD analysis (Figure 1c) revealed that the pristine Ge, Cu and Ge/Cu mixtures were transformed into Ge/germanium oxide (GeO_2), cuprous oxide (Cu_2O)/Cu and GeO_2/Cu_2O/Cu composite phases, respectively, during the preparation process. No Ge or GeO_2 characteristic peaks were detected in GeO_2/Cu_2O/Cu due to the low Ge content. Cross-sectional elemental mapping revealed a nanometer-scale catalyst layer thickness. The catalyst structure was analyzed by Raman spectroscopy (Figure 1d). The characteristic peaks of metallic Ge and GeO_2 at 294 and 437 cm^{-1}, and the vibrational peak at 144 cm^{-1} corresponds to the infrared active vibrational mode of Cu_2O [21–23]. The peak located at 214 cm^{-1} is the second-order octave vibrational peak of Cu_2O, while the peak at 635 cm^{-1} is attributed to the stretching vibration of the Cu-O bond in Cu_2O. These results are consistent with the XRD analysis. Electron Paramagnetic Resonance (EPR) spectra (Figure 1e) showed that the Ge/Cu catalysts exhibited the strongest spin-single-electron signals compared to pure Ge, indicating that the introduction of Ge significantly changed the oxidation state and coordination environment of Cu.

3.2. Electrocatalytic CO_2 Reduction to Ethanol over Ge/Cu-Catalyst

In order to investigate the mechanism of Ge modification on the ECR performance of Cu-based catalysts, a systematic test was carried out in 0.5 M $KHCO_3$ electrolyte using a two-compartment flow cell system separated by a Nafion 117 ion-exchange membrane in this study. Linear scanning voltammetry (LSV) tests showed the current response of the carbon paper substrate under CO_2 and Ar atmospheres almost overlapped (Figure 2a), confirming the absence of CO_2 reduction activity. In contrast, the Ge/Cu catalysts showed significantly higher current densities in CO_2 atmosphere than in Ar atmosphere in the potential range of −0.5 to −1.8 V vs. RHE, indicating significant ECR catalytic activity. Gas chromatography (GC) was used to detect the gaseous products, headspace sampler and ion chromatography to detect the liquid products, and the corresponding calibration curves are shown in Figures S7–S9. The Faraday efficiency (FE) of hydrogen (H_2) gradually decreased and the FE of carbon monoxide (CO) increased with the negative shift of potential for the pure Cu catalyst (Figure 2b), whereas, after the introduction of 15–20% Ge, the HER process was effectively suppressed and the FE of ethanol was enhanced by about 11–20% (Figures S10 and 2c). The Faradaic efficiencies of individual products at different applied potentials were summarized in Table S1. For the Ge/Cu catalyst, the Faradaic efficiency for ethanol reached a maximum of 47.8% at –0.8 V vs. RHE, representing an 11.2% increase compared to pure Cu. As the potential became more negative, the ethanol Faradaic efficiency of pure Cu decreased significantly, dropping to only 5.4% at –1.7 V vs. RHE, whereas the Ge/Cu catalyst maintained a relatively high efficiency of 25.9%, demonstrating superior potential stability and catalytic performance. Figure S11. Comparison of the catalytic performance of the Ge/Cu catalyst with previously reported catalysts, showing that its overall performance lies at a moderate level. The partial current densities of individual products were shown in Figure S12. The introduction of Ge resulted in a noticeable increase in the partial current density of ethanol. Electrochemical active surface area (ECSA) measurements (Figures 2d and S13) showed that Cu and Ge/Cu have similar ECSA values, unlike pure Ge, indicating that Ge enhances performance by modulating the intrinsic activity of catalytic sites rather than increasing their number (Table S2). As shown in Figure S14, Cu and Ge/Cu catalysts exhibited markedly different

Tafel slope behaviors during electrocatalytic CO_2 reduction to ethanol, revealing the intrinsic differences in their reaction pathways and stability. Based on the experimental results, we propose that the anomalous negative slope observed for the pure Cu catalyst arises from a potential-dependent "self-poisoning" effect: the excessive accumulation of strongly adsorbed CO intermediates blocked active sites, leading to a decrease in the ethanol formation rate and a concurrent increase in CO byproducts, resulting in a rapid decline in ethanol selectivity. In contrast, the positive slope of the Ge/Cu catalyst reflected normal reaction kinetics. The introduction of Ge modulated the electronic structure, optimized CO adsorption energy, prevented surface poisoning, and promoted the efficient conversion of CO intermediates into ethanol. Consequently, the Ge/Cu catalyst maintained high selectivity and stability over a wide potential range. This transition from a negative to a positive slope highlighted the critical role of intermediate adsorption regulation in achieving efficient and stable CO_2 electroreduction.

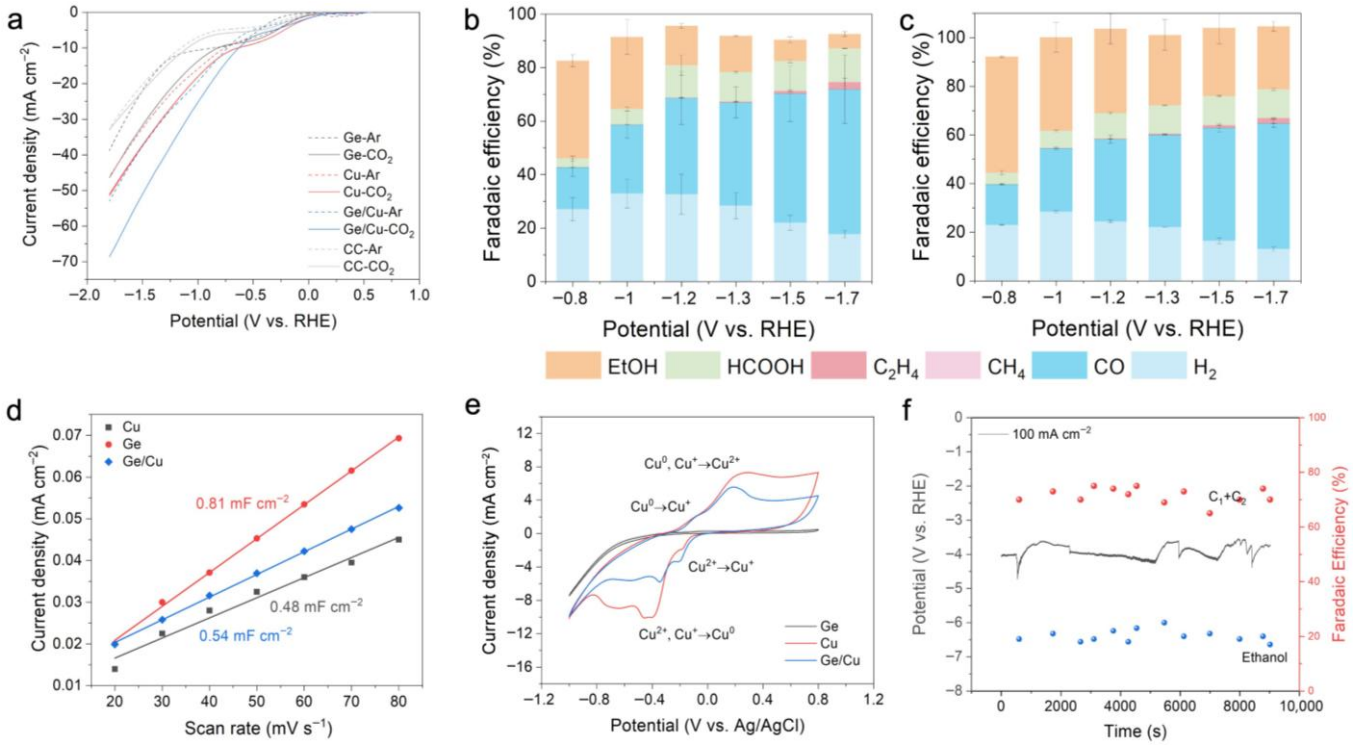

Figure 2. Potential-dependent electrocatalytic ECR performance. (**a**) LSV curves recorded at a scan rate of 10 mV s^{-1}, FEs of various products at different potentials for (**b**) Cu and (**c**) Ge/Cu, (**d**) Charging current density differences (Δj/2) versus scan rates, (**e**) CV curves after activation recorded at a scan rate of 50 mV s^{-1}, (**f**) Stability of Ge/Cu for ECR. All potentials were not iR-corrected.

No redox peaks were observed for Ge in the cyclic voltammetry (CV) curves in Figure 2e. In contrast, Cu and Ge/Cu exhibited significant reduction peaks in the potential range of −0.12 to −0.5 V vs. Ag/AgCl due to the reduction of Cu_xO to Cu. Two oxidation peaks at −0.16 to 0.29 V vs. Ag/AgCl were the oxidation of Cu to Cu^{1+} and Cu/Cu^{1+} to Cu^{2+}, respectively [24]. The activated Cu catalyst exhibited a higher current density than the pre-activated Cu, indicating the reduction of Cu_xO to Cu under negative potential, likely due to increased electronic conductivity. However, activated Ge/Cu electrodes showed lower current densities than before activation, suggesting that Ge modifies the Cu microenvironment and affects its oxidation state during electrolysis. To further prove the above conclusion, we performed electrochemical impedance tests (Figure S15). The solution impedance and charge transfer impedance of the Ge catalyst remained unchanged before and after ECR (Table S3). The impedance of Cu decreased after activation, consistent with the

increase in current density. This is in agreement with the previously reported conclusion in the literature that the dynamic evolution of electrocatalysts strongly depends on the conductivity. In contrast, although the impedance of Ge/Cu also decreased after activation, the current density declined, suggesting that the change may be attributed to the modulation of the surface microenvironment. Therefore, introducing an appropriate amount of Ge^{4+} to modulate the Cu^{+}/Cu^{0} ratio is essential. To systematically evaluate the stability of the Ge/Cu electrocatalysts, we performed constant potential durability tests using a flow cell in 0.5 M $KHCO_3$ electrolyte for more than 2.5 h. As shown in Figure 2f, the Ge/Cu catalyst demonstrated stable operation at a current density of 100 mA cm^{-2} without noticeable activity degradation. Remarkably, this test duration was not the ultimate lifetime of the catalyst, but was limited by the electrolytic cell configuration, especially the salinization phenomenon of GDE after continuous operation. Since the performance of Cu-based catalysts was closely related to their oxidation state, we preliminarily attributed the differences in catalytic behavior to variations in the microenvironment affecting Cu electroreduction.

Structural characterization of the catalyst after ECR testing revealed the dynamic evolution of the catalyst. The electronic structure and valence states of the catalysts were characterized in depth by X-ray photoelectron spectroscopy (XPS) (Figure S16). The Cu 2p spectrum analysis showed that both Cu and Ge/Cu catalysts before ECR testing showed characteristic peaks at 952.5 eV (2 $p_{1/2}$) and 932.5 eV (2 $p_{3/2}$), which were attributed to Cu^{0}/Cu^{1+} species [25]. The weak Cu^{2+} satellite peaks were also observed (Table S4), indicating the presence of a small number of Cu^{2+} species. Further analysis of the Cu Auger LMM spectrum confirmed that Cu^{0} (918.5 eV), Cu^{1+} (916.5 eV), and Cu^{2+} (917.6 eV) coexisted before the ECR, and this mixed valence may enhance the adsorption capacity of the *CO intermediate. Quantitative data on the $Cu^{0}/Cu^{1+}/Cu^{2+}$ ratios before and after the reaction were provided in Table S4. After the ECR reaction, Cu^{2+} in the Ge/Cu catalyst decreased significantly, being reduced to Cu^{0}, while the Cu^{1+} state remained stable. This indicated that the introduction of Ge effectively stabilized the Cu^{+} active sites. The Ge element remained in the +4 oxidation state, indicating that it existed in the form of GeO_2. The analysis of XRD patterns (Figure S17) showed the disappearance of the characteristic peaks of Ge and the appearance of the characteristic peaks of GeO_2 in the Ge/Cu catalysts. Raman spectrum (Figure S18) further confirmed the decrease in the crystallinity of the catalyst and the enhancement of the GeO_2 signal, which was consistent with the XRD results. By observing the SEM images after the ECR test, it was found that the bulk structure of the Ge catalyst (0.280 ± 1.68 μm) was maintained but underwent a size change, and the small cubes of the constituent units (initially 0.423 ± 0.208 μm) were fragmented into irregular particles (0.297 ± 0.085 μm) (Figure S19). The Cu catalyst maintained a spherical morphology (3.09 ± 1.70 μm) but reorganized into a secondary structure consisting of smaller nanorods (0.132 ± 0.05 μm) (Figure S20). The Ge/Cu catalyst showed a similar evolution, forming spherical aggregates of 0.324 ± 0.115 μm, with 0.093 ± 0.034 μm nanoparticles as the basic unit (Figure S21).

The Ge/Cu catalysts after ECR testing were characterized in depth by HRTEM. The Ge/Cu still maintains the initial core–shell structure (Figure S22). The facet spacing of 0.233 and 0.242 nm corresponds to the (012) and (110) facets of GeO_2, respectively. The crystal plane spacings of 0.213 and 0.301 nm perfectly match the (200) and (110) crystal planes of Cu_2O. These measurements of the interplanar spacing were highly consistent with the analytical results of the SAED profile, together confirming the coexistence of GeO_2 and Cu_2O in the catalyst. Notably, the thickness of the interfacial oxide layer of the core–shell structure increased by 30.9 nm (the total thickness reached 103.2 nm.) The EDS elemental mapping showed that the elements of Cu, Ge, and O were stably present and uniformly distributed. The above results indicate that the catalysts underwent significant

morphological fragmentation and reorganization and structural refinement under the effect of electrochemical reaction and electric field. This dynamic evolution may have an important impact on its catalytic performance. The defect sites of the catalysts were investigated by Pb underpotential deposition technique (Figure S23). Both Cu and Ge/Cu samples showed an anodic characteristic peak at −0.16 V (vs. Ag/AgCl), while pure Ge did not have this response. The intensity of this peak showed a volcano-type trend with increasing Ge doping, indicating that Ge doping did not form a high density of undercoordinated sites, but instead moderately reduced the unsaturated coordination defects of Cu. The highly consistent results of five consecutive cyclic tests confirm the reliability of the phenomenon. These findings indicated that the electronic structure of Cu could be optimized by precisely controlling the Ge doping amount, which could significantly enhance the ECR performance of Cu catalysts.

3.3. Investigation of Reaction Mechanism

The reaction mechanism of Ge/Cu catalysts was revealed by in situ attenuated total reflection Fourier transform infrared spectroscopy (ATR-FTIR) studies (Figure 3). During the ECR process, characteristic absorption peaks were detected at 1860–1900 cm^{-1} (*CO_{bridge}) and 2040–2080 cm^{-1} (*CO_{atop}) for both Cu and Ge/Cu catalysts, confirming the CO_2 activation and the formation of *CO intermediates [26,27]. The presence of both *CO_{atop} and *CO_{bridge} structures on the Cu catalyst, with peak intensities increasing and then decreasing with a negative shift in potential, suggests an accelerated rate of *CO consumption at higher potentials (Figure 3a). However, the Ge/Cu catalysts exhibited significantly different adsorption characteristics, with the *CO_{bridge} structure dominating and the signal intensity continuously enhanced, while the *CO_{atop} signal was always weak (Figure 3b). This unique *CO adsorption mode not only effectively inhibits HER, but more importantly promotes C-C coupling.

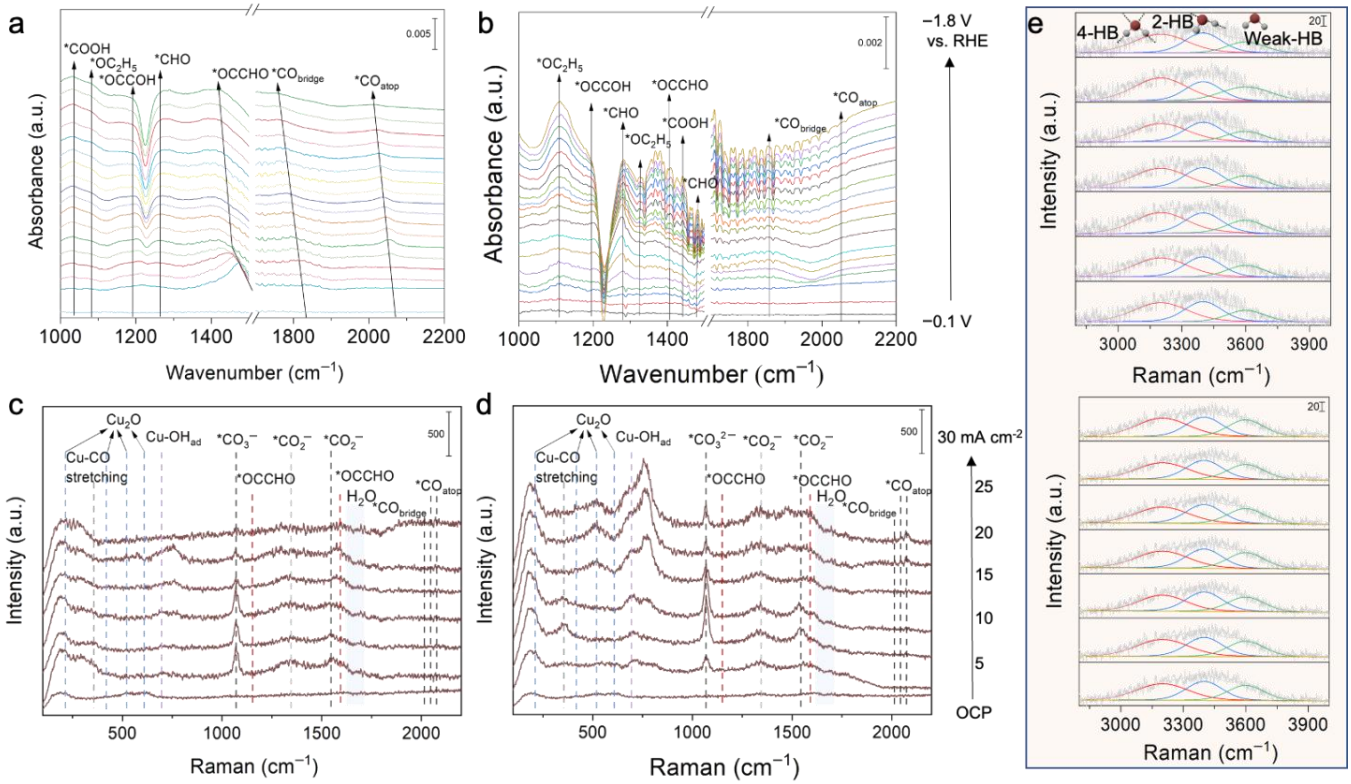

Figure 3. Potential-dependent in situ IR spectrum of (**a**) Cu and (**b**) Ge/Cu; Current density-dependent in situ Raman spectrum of (**c**) Cu, (**d**) Ge/Cu, and (**e**) water molecule analyses at the

electrode/electrolyte interfaces (Cu catalyst on top and Ge/Cu catalyst on bottom). Green represents Weak-HB, blue represents 2-HB, and red represents 4-HB.

In addition to the $*CO_{atop}$ and $*CO_{bridge}$ characteristic peaks, the adsorption peaks of *CHO intermediates were observed in the in situ ATR-FTIR plots, indicating that the Ge/Cu catalysts preferred the formation of *COCHO (or *COCOH) intermediates via the asymmetric coupling of $*CO_{bridge}$ to *CHO (or *COH). This coupling pathway is thermodynamically more favorable than *CO dimerization, effectively enhancing the selectivity of the C_2 product. Notably, the detection of *OCCOH and *OCCHO intermediates at 1328 and 1080 cm^{-1} confirms the C-C coupling process, while the $*OC_2H_5$ characteristic peaks provide direct evidence for the ethanol generation pathway [28,29]. Crucially, the intensity of the $*OC_2H_5$/*OCCOH peaks on the surface of the Ge/Cu catalyst was significantly higher than that of Cu, suggesting that the introduction of Ge stabilized the key intermediates of ethanol through two mechanisms: promoting the symmetric coupling of *CO and simultaneously inducing the asymmetric coupling of *CO with *CHO (or *COH). This dual action not only inhibits the generation of ethylene by-products, but also is highly consistent with the mechanism of "synergistic promotion of C_2 alcohols formation by multiple active sites" reported in the literature, which perfectly explains the phenomenon of ethanol selectivity enhancement observed in the experiments [30,31].

We further verified the modulation mechanism of Ge on Cu catalysts by in situ Raman spectroscopy analysis (Figure 3c,d). Compared with Cu, the Ge/Cu catalyst showed stronger Cu_2O characteristic peaks at about 419, 521, and 606 cm^{-1}, among which the intensity of the peak at 521 cm^{-1} was enhanced with the increase in the current density, confirming that Ge effectively stabilized the Cu^{1+} species [32–34]. Notably, the Cu-CO stretching vibrational peak at 354.7 cm^{-1} was more intense on Ge/Cu but eventually disappeared [35], while the $Cu\text{-}OH_{ad}$ peak at 693 cm^{-1} was continuously enhanced, indicating that Ge changed the catalyst surface microenvironment. In particular, the $*CO_3^{2-}$ peak at 1070 cm^{-1} decried more slowly on Ge/Cu, confirming that Ge maintains a localized alkaline environment, which facilitates C-C coupling [36]. In addition, more pronounced $*CO_{atop}$ and $*CO_{bridge}$ signals as well as detected *OCCHO intermediates were observed on Ge/Cu than on Cu, in perfect agreement with the in situ ATR-FTIR results. Together, these two in situ characterizations confirm the possible simultaneous occurrence of the *CO symmetric coupling promoted by Ge and the asymmetric coupling mechanism of *CO with CHO (or *COH), which may be a key factor in enhancing the selectivity of the C_2 product. The molecular structure of water at the electrode/electrolyte interface was thoroughly investigated by in situ Raman spectroscopy (Figure 3e). The O-H stretching vibration (νO-H) in the range of 3000–3800 cm^{-1} can be categorized into three characteristic peaks, 3200 cm^{-1} (four-coordinated hydrogen-bonded water, 4-HB), 3400 cm^{-1} (two-coordinated hydrogen-bonded water, 2-HB) [25,26] and 3600 cm^{-1} (weak hydrogen-bonded dangling O-H) [37,38]. The frequency of these peaks varies significantly with the applied potential (or current density), confirming that the detected signal originates from interfacial water within the molecular layer on the catalyst surface. Notably, the weak-HB water signal was markedly enhanced on the Ge/Cu catalyst. As reported, the activation energy for water dissociation follows the order: weak-HB < 2-HB < 4-HB. Therefore, the enrichment of weak-HB water on the Ge/Cu surface facilitates *H formation. This correlates well with the excellent ECR performance of Ge/Cu and highlights the critical role of interfacial water structure in promoting efficient catalysis.

3.4. Density Functional Theory (DFT) Calculations

By using density-functional theory (DFT) calculations, we revealed the mechanism of electronic structure modulation of Cu catalysts by Ge^{4+}. The Calculations showed that

introducing Ge^{4+} shifted the Cu_2O d-band center upward from –1.539 eV to –1.499 eV (Figure 4a), closer to the Fermi level, thereby significantly influencing the adsorption of key intermediates. In the $Cu/Cu_2O/GeO_2$ composite formed under cathodic conditions, the *CO adsorption energy decreased from –0.55 eV to –0.62 eV, consistent with enhanced *CO adsorption observed via in situ Raman and ATR-FTIR (Figure 4b,c). Meanwhile, the Gibbs free energy of *H increased slightly from 0.09 eV to 0.11 eV, effectively suppressing HER. These calculations demonstrated that the enhanced ECR performance of the Ge/Cu catalysts originated from strengthened *CO adsorption, which facilitated C–C coupling, and a moderate increase in *H binding energy, which effectively suppressed the HER, thereby collectively improving C_{2+} product selectivity.

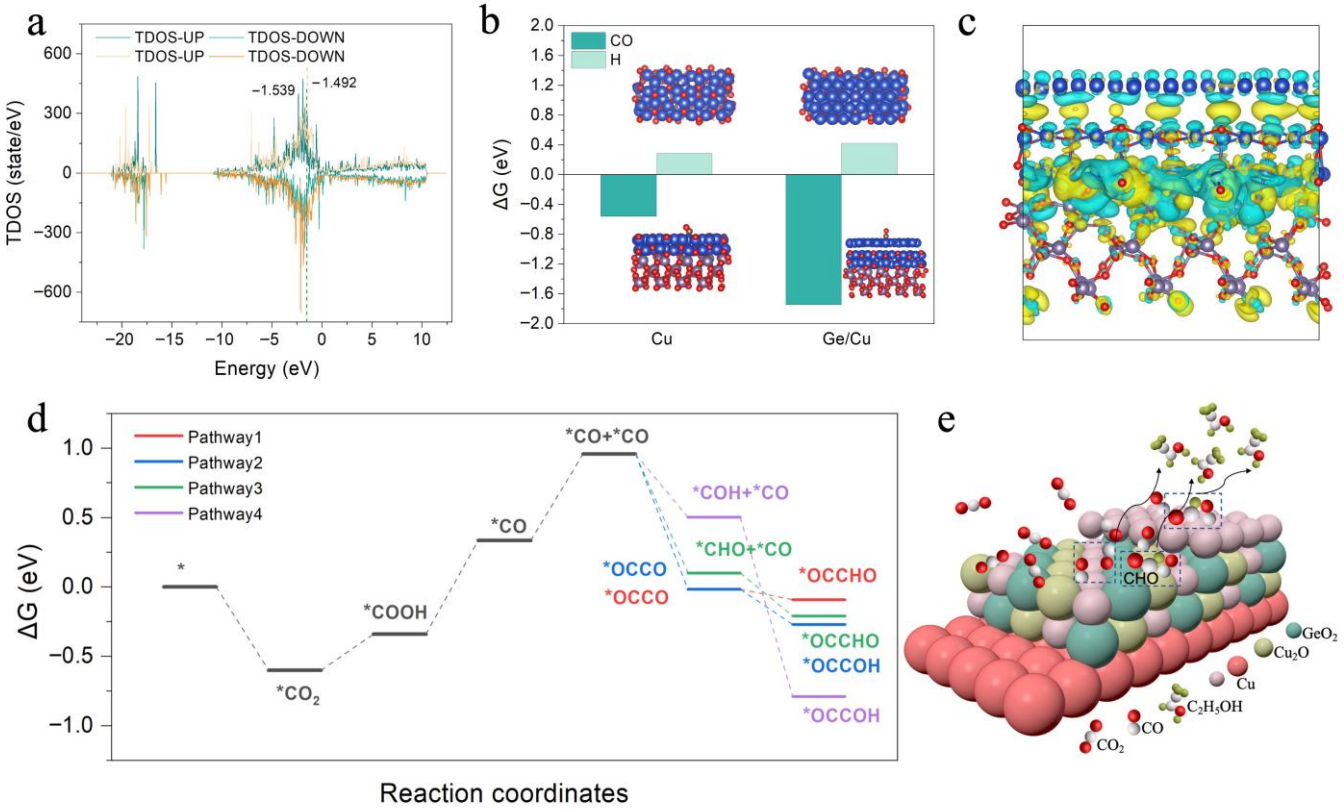

Figure 4. (**a**) Information for electron property of different active sites, including the density of states and band center of Cu and Ge/Cu, (**b**) the adsorption energy comparisons of CO and H on different sites of Ge/Cu, (**c**) differential charge density of Ge/Cu, (**d**) the ECR energy diagram showing the pathways alongside the key intermediates toward the different C_2 products on Ge/Cu, (**e**) Schematic illustration of the ethanol formation mechanism.

Based on the *COOH intermediate detected by ATR-FTIR spectroscopy, we elucidated the CO_2-to-C_2 product formation mechanism using DFT calculations (Figure 4d). According to the widely accepted ECR pathway, CO_2 is first reduced to *CO via *COOH, followed by C–C coupling as the rate-determining step. Theoretical calculations identified two primary pathways: (1) symmetric *CO dimerization (*CO + *CO → *OCCO → *OCCHO/*OCCOH) with a barrier of 0.97 eV; and (2) asymmetric coupling, where *CO is first hydrogenated to *CHO (0.46 eV) or *COH (0.86 eV), then coupled with *CO to form *OCCHO (0.31 eV) or *OCCOH (1.28 eV). Gibbs free energy analysis showed that the asymmetric coupling of *CO + *CHO carried out after the hydrogenation of *CO to form *CHO was thermodynamically significantly superior to the symmetric dimerization pathway (0.97 eV), which was in perfect agreement with the characteristics of the *CHO

intermediates and the asymmetric coupling observed by in situ Raman and ATR-FTIR. These results collectively confirm that the Ge/Cu catalyst surface prefers the selective generation of C_2 products via the asymmetric coupling pathway of *CO → *CHO → *OCCHO. Figure 4e presents a schematic illustration of the ethanol formation pathway, highlighting the key intermediates and the asymmetric coupling steps responsible for the high C_{2+} selectivity.

4. Conclusions

In this study, the efficient catalytic mechanism of Ge-modified Cu-based catalysts for ECR was elucidated through systematic experiments, advanced characterizations, and DFT calculations. Experimental results revealed that Ge incorporation formed a stable core–shell structure, stabilized Cu^{1+} species, and modulated oxygen vacancy concentration, thereby optimizing the active sites. In situ infrared and Raman spectroscopy confirmed that unique $*CO_{bridge}$ and $*CO_{atop}$ adsorption modes on the Ge/Cu surface promoted the asymmetric *CO–*CHO coupling pathway. DFT calculations further clarified that Ge^{4+} doping shifted the Cu_2O d-band center upward, enhancing *CO adsorption and significantly lowering the energy barriers for asymmetric coupling compared to symmetric dimerization. In addition, in situ Raman spectroscopy revealed that Ge induced a locally alkaline microenvironment and enriched weakly hydrogen-bonded water, further promoting C–C coupling and suppressing the HER. This multilevel modulation strategy improved the ethanol Faradaic efficiency of the Ge/Cu catalyst by 11–20%. In future studies, longer-term stability tests will be conducted, and the reactor design and ink formulation will be further optimized to systematically investigate the long-term stability of the catalyst. Overall, this work proposes a novel approach to simultaneously tuning the electronic structure, intermediate adsorption, and interfacial microenvironment via heteroatom doping, offering new insights for designing efficient C_{2+} product catalysts.

Supplementary Materials: The following supporting information can be downloaded at: https://www.mdpi.com/article/10.3390/app152111420/s1, Figure S1. SEM images of Ge-GDE, (a,b) top view, (c) elemental mapping, (d) EDS image, (e,f) elemental mapping images from a lateral view, (g,h) Particle size distribution image. Figure S2. SEM images of Cu-GDE, (a,b) top view, (c,d) elemental mapping, (e) EDS image, (f) elemental mapping images from a lateral view, (g) Particle size distribution image. Figure S3. SEM images of Ge/Cu-GDE, (a,b) top view, (c-f) elemental mappings, (g-i) elemental mapping images from a lateral view, (j) EDS image, (h) Particle size distribution image. Figure S4. SEM images of 10 wt% Ge/Cu-GDE, (a, b) top view, (c-e) elemental mappings, (f) EDS image, (g-i) elemental mapping images from a lateral view. Figure S5. SEM images of 20 wt%Ge/Cu-GDE, (a, b) top view, (c-f) elemental mappings, (g-i) elemental mapping images from a lateral view, (j) EDS image. Figure S6. (a) EDS image, (b) SAED image and (c) corresponding element mappings of Ge/Cu. Figure S7. Method for quantification of liquid products concentration. Calibration curves for (a) H_2, (b) CH_4, and (c) C_2H_4 in gas chromatography, respectively. Figure S8. Method for quantification of liquid products concentration. Calibration curves for (a) HCOOH and (b)CH_3COOH in ion chromatography, respectively. Figure S9. Method for quantification of liquid products concentration. Calibration curves for (a) CH_3OH, (b) EtOH, and (c) n-PrOH in GC with headspace sampler, respectively. Figure S10. FEs of various products at different potentials for (a) 5 wt% Ge/Cu, (b) 10 wt% Ge/Cu, (c) 20 wt% Ge/Cu and (d) 30 wt% Ge/Cu. Figure S11. Comparison of the catalytic performance of Ge/Cu with reported catalysts [39–46]. Figure S12. Partial current density of Cu and Ge/Cu catalysts for individual products. Figure S13. Double-layer capacitances: (a) Ge, (b) Cu, (c) 5 wt%Ge/Cu, (d) 10 wt%Ge/Cu, (e) Ge/Cu, (f) 20 wt%Ge/Cu, (g) 30 wt%Ge/Cu, (h) Charging current density differences ($\Delta j/2$) versus scan rates (20–80 mV s^{-1}). The electrodes are first pre-reduced in 0.5 M $KHCO_3$ at 50 mA cm^{-2} for 30 min. Figure S14. Partial current density of Cu and Ge/Cu catalysts for individual products. Figure S15. EIS plots before and after the ECR process. The

full circles represent the data obtained after the ECR measurement, while the empty circles correspond to the data recorded before the ECR measurement. Figure S16. XPS characterization of surface composition for Cu and Ge/Cu before and after ECR test: (a) Cu 2p, (b) Cu LMM, (c) O 1s, (d) Ge 3d spectrum. Figure S17. XRD patterns after ECR test. Figure S18. Raman spectroscopy after ECR test. Figure S19. SEM images of Ge/GDE after ECR test, (a, b) SEM images, (c) elemental mapping, (d, e) Particle size distribution image, (f) EDS image. Figure S20. SEM images of Cu-GDE after ECR test, (a, b) SEM images, (c) elemental mapping, (d, e) Particle size distribution image, (f) EDS image. Figure S21. SEM images of Ge/Cu-GDE after ECR test, (a, b) top view, (c) elemental mapping images from a lateral view, (d, e) Particle size distribution image. Figure S22. Structural characterization of 15%Ge-Cu after ECR: (a) TEM image, (b) HRTEM image, (c) corresponding SAED pattern, (d) EDS element mappings. Figure S23. Pb underpotential deposition (UPD) tests were performed at a scan rate of 10 mV s^{-1} in a solution containing 0.1 M $NaClO_4$, 10 mM $HClO_4$, and 3 mM $Pb(ClO_4)_2$: (a) Cu and Ge, (b) 5 wt% Ge/Cu, (c) 10 wt% Ge/Cu, (d) Ge/Cu, (e) 20 wt% Ge/Cu, and (f) 30 wt% Ge/Cu. All samples were activated by ECR for 1 h at a current density of 20 mA cm^{-2}. Table S1 Faradaic efficiencies of individual products at different applied potentials. Table S2 ECSA value of catalysts. Table S3 Experimental and simulated EIS values of the electrocatalysts before and after the ECR process. Table S4 Surface elemental composition determined by XPS.

Author Contributions: Conceptualization, B.D.; Formal analysis, X.L., L.W., H.X., Z.L., X.D. and B.D.; Funding acquisition, L.W., H.X. and B.D.; Investigation, X.L., L.W., H.X., Z.L., X.D. and B.D.; Methodology, X.L., L.W., H.X. and B.D.; Resources, X.L., L.W., H.X. and Z.L.; Validation, X.L., L.W. and B.D.; Writing – original draft, X.L.; Writing – review & editing, X.L., L.W. and B.D. All authors have read and agreed to the published version of the manuscript.

Funding: This work was funded by the "Pioneer" and "Leading Goose" R&D Program of Zhejiang (No. 2023C03017), China Postdoctoral Science Foundation (No. GZC20230373), Natural Science Foundation of Huzhou City (No. 2024YZ19), National Natural Science Foundation of China (No. 22406020), Zhejiang Provincial Natural Science Foundation of China (No. LQ24B070010), CMA Key Open Laboratory of Transforming Climate Resources to Economy (No. 2024004K), Young Leader Talent Development Program of Yangtze Delta Region Institute (Huzhou) of UESTC (No. RC0324001901).

Institutional Review Board Statement: Not applicable.

Informed Consent Statement: Not applicable.

Data Availability Statement: Data will be made available on request.

Conflicts of Interest: The authors declare that they have no known competing financial interests or personal relationships that could have appeared to influence the work reported in this paper.

References

1. Ahmed, S.; Khan, M.K.; Kim, J. Revolutionary advancements in carbon dioxide valorization via metal-organic framework-based strategies. *Carbon Capture Sci. Technol.* **2025**, *15*, 100405.
2. Ahmed, S.; Hussain, M.S.; Khan, M.K.; Kim, J. Innovations in catalysis towards efficient electrochemical reduction of CO_2 to C_1 chemicals. *J. Energy Chem.* **2025**, *107*, 622–649.
3. Ye, Q.; Zhao, X.; Jin, R.; Dong, F.; Xie, H.; Deng, B. Advances and challenges in membrane electrode assembly electrolyzers for CO_2 reduction. *J. Mater. Chem. A* **2023**, *11*, 21498–21515.
4. Deng, B.; Huang, M.; Zhao, X.; Mou, S.; Dong, F. Interfacial electrolyte effects on electrocatalytic CO_2 reduction. *ACS Catal.* **2021**, *12*, 331–362.
5. Lv, H.; Lv, F.; Qin, H.; Min, X.; Sun, L.; Han, N.; Xu, D.; Li, Y.; Liu, B. Single-crystalline mesoporous palladium and palladium-copper nanocubes for highly efficient electrochemical CO_2 reduction. *CCS Chemistry* **2022**, *4*, 1376–1385.
6. Deng, B.; Zhao, X.; Li, Y.; Huang, M.; Zhang, S.; Dong, F. Active site identification and engineering during the dynamic evolution of copper-based catalysts for electrocatalytic CO_2 reduction. *Sci.China Chem.* **2022**, *66*, 78–95.

7. Liu, M.; Wang, Q.; Luo, T.; Herran, M.; Cao, X.; Liao, W.; Zhu, L.; Li, H.; Stefancu, A.; Lu, Y.R.; et al. Potential alignment in tandem catalysts enhances CO_2-to-C_2H_4 conversion efficiencies. *J. Am. Chem. Soc.* **2024**, *146*, 1, 468–475.
8. Zhang, X.Y.; Lou, Z.X.; Chen, J.; Liu, Y.; Wu, X.; Zhao, J.Y.; Yuan, H.Y.; Zhu, M.; Dai, S.; Wang, H.F.; et al. Direct OC-CHO coupling towards highly C_{2+} products selective electroreduction over stable Cu^0/Cu^{2+} interface. *Nat. Commun.* **2023**, *14*, 7681.
9. Su, X.; Jiang, Z.; Zhou, J.; Liu, H.; Zhou, D.; Shang, H.; Ni, X.; Peng, Z.; Yang, F.; Chen, W.; et al. Complementary operando spectroscopy identification of in-situ generated metastable charge-asymmetry Cu_2-CuN_3 clusters for CO_2 reduction to ethanol. *Nat. Commun.* **2022**, *13*, 1322.
10. Deng, B.; Huang, M.; Li, K.; Zhao, X.; Geng, Q.; Chen, S.; Xie, H.; Dong, X.; Wang, H.; Dong, F. The crystal plane is not the key factor for CO_2-to-methane electrosynthesis on reconstructed Cu_2O microparticles. *Angew. Chem. Int. Ed.* **2022**, *61*, e202114080.
11. Lian, Z.; Dattila, F.; López, N. Stability and lifetime of diffusion-trapped oxygen in oxide-derived copper CO_2 reduction electrocatalysts. *Nat. Catal.* **2024**, *7*, 401–411.
12. Feng, J.; Wu, L.; Liu, S.; Xu, L.; Song, X.; Zhang, L.; Zhu, Q.; Kang, X.; Sun, X.; Han, B. Improving CO_2-to-C_{2+} product electroreduction efficiency via atomic lanthanide dopant-induced tensile-Strained CuO_x catalysts. *J. Am. Chem. Soc.* **2023**, *145*, 9857–9866.
13. Xu, L.; Feng, J.; Wu, L.; Song, X.; Tan, X.; Zhang, L.; Ma, X.; Jia, S.; Du, J.; Chen, A.; et al. Identifying the optimal oxidation state of Cu for electrocatalytic reduction of CO_2 to C_{2+} products. *Green Chem.* **2023**, *25*, 1326–1331.
14. Liu, C.; Guo, R.-T.; Zhu, H.-W.; Cui, H.-F.; Liu, M.-Y.; Pan, W.-G. Cu_2O-based catalysts applied for electrocatalytic CO_2 reduction: A review. *J. Mater. Chem. A* **2024**, *12*, 31769–31796.
15. Fan, Q.; Zhang, X.; Ge, X.; Bai, L.; He, D.; Qu, Y.; Kong, C.; Bi, J.; Ding, D.; Cao, Y.; et al. Manipulating Cu nanoparticle surface oxidation states tunes catalytic selectivity toward CH_4 or C_{2+} products in CO_2 electroreduction. *Adv. Energy Mater.* **2021**, *11*, 2101424.
16. Jia, B.; Li, L.; Xue, C.; Kang, J.; Liu, L.M.; Guo, T.; Wang, Z.; Huang, Q.; Guo, S. Restraining interfacial Cu^{2+} by using amorphous SnO_2 as sacrificial Protection boosts CO_2 electroreduction. *Adv. Mater.* **2023**, *35*, e2305587.
17. Jiang, Y.; Wang, X.; Duan, D.; He, C.; Ma, J.; Zhang, W.; Liu, H.; Long, R.; Li, Z.; Kong, T.; et al. Structural reconstruction of Cu_2O superparticles toward electrocatalytic CO_2 reduction with high C_{2+} products selectivity. *Adv. Sci.* **2022**, *9*, e2105292.
18. Xu, H.; Rebollar, D.; He, H.; Chong, L.; Liu, Y.; Liu, C.; Sun, C.-J.; Li, T.; Muntean, J.V.; Winans, R.E.; et al. Highly selective electrocatalytic CO_2 reduction to ethanol by metallic clusters dynamically formed from atomically dispersed copper. *Nat. Energy* **2020**, *5*, 623–632.
19. Yue, K.; Qin, Y.; Huang, H.; Lv, Z.; Cai, M.; Su, Y.; Huang, F.; Yan, Y. Stabilized Cu^0 -Cu^{1+} dual sites in a cyanamide framework for selective CO_2 electroreduction to ethylene. *Nat. Commun.* **2024**, *15*, 7820.
20. Yang, X.; Cheng, J.; Yang, X.; Xu, Y.; Sun, W.; Zhou, J. MOF-derived Cu@Cu_2O heterogeneous electrocatalyst with moderate intermediates adsorption for highly selective reduction of CO_2 to methanol. *Chem. Eng. J.* **2022**, *431*, 134171.
21. Han, M.; Liu, J.; Zheng, K.; Deng, C.; Mu, Y.; Guo, J.; Chu, Y.; Zou, Z.; Yu, F.; Li, W.; et al. Pressure-induced dense and robust Ge architecture for superior volumetric lithium storage. *Adv. Energy Mater.* **2024**, *14*, 2401065.
22. Ouyang, J.; Feng, C.; Ji, X.; Li, L.; Gutti, H.K.; Kim, N.Y.; Artzi, D.; Xie, A.; Kong, N.; Liu, Y.N.; et al. 2D monoelemental germanene quantum dots: Synthesis as robust photothermal agents for photonic cancer nanomedicine. *Angew. Chem. Int. Ed. Engl.* **2019**, *58*, 13405–13410.
23. Yan, S.; Song, H.; Lin, S.; Wu, H.; Shi, Y.; Yao, J. GeO_2 encapsulated Ge nanostructure with enhanced lithium-storage properties. *Adv. Funct. Mater.* **2019**, *29*, 1807946.
24. Min, S.; Xu, X.; He, J.; Sun, M.; Lin, W.; Kang, L. Construction of cobalt porphyrin-modified Cu_2O nanowire array as a tandem electrocatalyst for enhanced CO_2 reduction to C_2 products. *Small* **2024**, *20*, e2400592.
25. Li, P.; Bi, J.; Liu, J.; Zhu, Q.; Chen, C.; Sun, X.; Zhang, J.; Han, B. In situ dual doping for constructing efficient CO_2-to-methanol electrocatalysts. *Nat. Commun.* **2022**, *13*, 1965.
26. Chou, T.C.; Chang, C.C.; Yu, H.L.; Yu, W.Y.; Dong, C.L.; Velasco-Velez, J.J.; Chuang, C.H.; Chen, L.C.; Lee, J.F.; Chen, J.M.; et al. Controlling the oxidation state of the Cu electrode and reaction intermediates for electrochemical CO_2 reduction to ethylene. *J. Am. Chem. Soc.* **2020**, *142*, 2857–2867.
27. Kim, J.; Lee, T.; Jung, H.D.; Kim, M.; Eo, J.; Kang, B.; Jung, H.; Park, J.; Bae, D.; Lee, Y.; et al. Vitamin C-induced CO_2 capture enables high-rate ethylene production in CO_2 electroreduction. *Nat. Commun.* **2024**, *15*, 192.
28. Qiao, Y.; Shen, S.; Mao, C.; Xiao, Y.; Lai, W.; Wang, Y.; Zhong, X.; Lu, Y.; Li, J.; Ge, J.; et al. Interfacial oxygen vacancy-copper pair sites on inverse CeO_2/Cu catalyst enable efficient CO_2 electroreduction to ethanol in acid. *Angew. Chem. Int. Ed. Engl.* **2025**, *64*, e202424248.

29. Li, S.; Wu, G.; Mao, J.; Chen, A.; Liu, X.; Zeng, J.; Wei, Y.; Wang, J.; Zhu, H.; Xia, J.; et al. Tensile-strained Cu penetration electrode boosts asymmetric C-C coupling for ampere-level CO_2-to-C_{2+} reduction in acid. *Angew. Chem. Int. Ed. Engl.* **2024**, *63*, e202407612.
30. Wang, S.; Li, F.; Zhao, J.; Zeng, Y.; Li, Y.; Lin, Z.Y.; Lee, T.J.; Liu, S.; Ren, X.; Wang, W.; et al. Manipulating C-C coupling pathway in electrochemical CO_2 reduction for selective ethylene and ethanol production over single-atom alloy catalyst. *Nat. Commun.* **2024**, *15*, 10247.
31. Wang, R.; Dong, L.-Z.; Shi, J.-W.; Zhang, M.; Li, S.-L.; Lan, Y.-Q.; Liu, J. Switching the symmetry of a trinuclear copper cluster catalyst for electroreducing CO_2 to an asymmetric C_2 product in an acidic electrolyte. *ACS Catal.* **2024**, *14*, 741–750.
32. de Ruiter, J.; Benning, V.R.M.; Yang, S.; den Hartigh, B.J.; Wang, H.; Prins, P.T.; Dorresteijn, J.M.; Janssens, J.C.L.; Manna, G.; Petukhov, A.V.; et al. Multiscale X-ray scattering elucidates activation and deactivation of oxide-derived copper electrocatalysts for CO_2 reduction. *Nat. Commun.* **2025**, *16*, 373.
33. Ma, X.; Xu, L.; Liu, S.; Zhang, L.; Tan, X.; Wu, L.; Feng, J.; Liu, Z.; Sun, X.; Han, B. Electrochemical C-C coupling between CO_2 and formaldehyde into ethanol. *Chem Catal.* **2022**, *2*, 3207–3224.
34. Zou, Y.; Wang, S. An investigation of active sites for electrochemical CO_2 reduction reactions: From in situ characterization to rational design. *Adv. Sci.* **2021**, *8*, 2003579.
35. Lu, X.; Wang, L.; Zhao, X.; Pan, B.; Li, Z.; Du, X.; Zhang, S.; Dong, F.; Deng, B. Unlocking asymmetric C-C coupling pathways on commercial Cu catalysts *via* Cu (100) grain boundaries for efficient and durable CO electroreduction. *Chinese J. Catal.* **2025**, *76*, 198–209.
36. Li, H.; Wei, P.; Gao, D.; Wang, G. In situ Raman spectroscopy studies for electrochemical CO_2 reduction over Cu catalysts. *Curr. Opin. Green Sust.* **2022**, *34*, 100589.
37. Zou, C.J.; Du, Z.Y.; Tang, W.; Liu, Q.; Liu, X.B.; Dong, J.C.; Fang, P.P.; Li, J.F. Interfacial water on Ag/Ag_2S nanowires enhancing the ethanol selectivity for CO_2 electroreduction. *Adv. Mater.* **2025**, *37*, 2503010.
38. He, X.; Lin, L.; Li, X.; Zhu, M.; Zhang, Q.; Xie, S.; Mei, B.; Sun, F.; Jiang, Z.; Cheng, J.; et al. Roles of copper(I) in water-promoted CO_2 electrolysis to multi-carbon compounds. *Nat. Commun.* **2024**, *15*, 9923.
39. Sun L.; Zheng X.; Li Y.; Lin M.; Zeng X.; Yu J.; Song Z.; Zhang L. Nanoconfinement and tandem catalysis over yolk-shell catalysts towards electrochemical reduction of CO_2 to multi-carbon products. *J. Colloid Interface Sci.* **2025**, 687, 733-741.
40. Yang C.; Wang R.; Yu C.; Xiao J.; Huang Z.; Lv B.; Zhao H.; Wu X.; Jing G. Engineering stable Cu^{+}-Cu^{0} sites and oxygen defects in boron-doped copper oxide for electrocatalytic reduction of CO_2 to C_{2+} products. *Chem. Eng. J.,* **2024**, 484, 149710.
41. Wang R.; Liu Y.; Kong Y.; Chen Q.; Zhao S. Stabilization of Cu_2O catalyst via strong electronic interaction for selective electrocatalytic CO_2 reduction to ethanol. *Chem. Eng. J.,* **2024**, 499, 156065.
42. Jin P.; Wang Q.; Gu X.; Huang L.; Qin W.; Chong Y.; Pruksawan S.; Zhang S.; Wang F.; Lin X. MOFs derived N doped CuNix@C dual metallic core-shell electrocatalysts for CO_2 electrocatalytic reduction. *Int. J. Electrochem. Sc.,* **2024**, 19, 100427.
43. Da Y.; Chen J.; Fan L.; Jiang R.; Xiao Y.; Wang M.; Chen G.; Tian Z.; Zhang H.; Jin H.; Chen X.; Ji C.; Xi S.; Lum Y.; Wang L.; Zhu T.; Zhang J.; Chen W. Selective and energy efficient electrocatalytic CO_2-to-ethanol conversion through anion modulation. *Angew. Chem. Int. Ed. Engl.,* **2025**, 64, e202506867.
44. Liu X.; Ma Y.; Song Q.; Huang H.; He Y.; Sun S.; Wang Z. Direct observation of surface-bound intermediates in CO/CO_2 reduction on a polycrystalline Cu electrode using broad-band SFG spectroscopy. *J. Phys. Chem. C,* **2023**, 127, 23675-23686.
45. Yu Z.; Gu M.; Wang H.; Jiang L.; Sun P.; Liu X.; Pei Y.; Wang G.; Zhang X. Dual sites on graphitic biochar for electrocatalytic CO_2 reduction to ethanol conversion. *J. Phys. Chem. C,* **2024**, 128, 4171-4179.
46. Angerasa F. T.; Moges E. A.; Chang C.-Y.; Lakshmanan K.; Dessie T. A.; Huang W.-H.; Edao H. G.; Dilebo W. B.; Guta C. B.; Chang C.-C.; Liao W.-S.; Shen J.; Habtu N. G.; Tsai M.-C.; Su W.-N.; Hwang B. J. Selective electrochemical reduction of CO_2 to ethanol on a heteroatom-coordinated dual-atom catalyst of Fe/Cu-NC. *Chem. Mater.,* **2025**, 37, 2474-2484.

Disclaimer/Publisher's Note: The statements, opinions and data contained in all publications are solely those of the individual author(s) and contributor(s) and not of MDPI and/or the editor(s). MDPI and/or the editor(s) disclaim responsibility for any injury to people or property resulting from any ideas, methods, instructions or products referred to in the content.